

RESEARCH ARTICLE

10.1029/2018JB015626

Muon Tomography Applied to a Dense Uranium Deposit at the McArthur River Mine

Douglas Schouten¹ and Patrick Ledru²

¹CRM Geotomography Technologies, Inc., Vancouver, British Columbia, Canada, ²Areva Resources Canada, Inc., Saskatoon, Saskatchewan, Canada

Key Points:

- Muon tomography can be used for imaging density contrasts deep underground
- Muon tomography imaging is applicable to exploration of compact uranium deposits
- Three-dimensional inversion for density from muon tomography data corresponds well to the density profile extracted from drill assay data

Correspondence to:

D. Schouten, dschouten@crmtgm.com

Citation:

Schouten, D. W., & Ledru, P. (2018). Muon tomography applied to a dense uranium deposit at the McArthur River mine. *Journal of Geophysical Research: Solid Earth*, 123. <https://doi.org/10.1029/2018JB015626>

Received 24 OCT 2017

Accepted 30 SEP 2018

Accepted article online 4 OCT 2018

Abstract This article reports on the first application of muon tomography (a novel method for imaging density contrasts underground using cosmic rays) for imaging dense uranium deposits within the Athabasca Basin in Canada. We present a qualitative assessment of the radiographic imaging and 3-D density inversion of a uranium deposit using muon tomography. The muon tomography survey summarized in this article was performed at the McArthur River mine. We demonstrate the validity of muon tomographic imaging with data acquired at a depth of about 600 m underground. The statistical significance of the uranium deposit signature in the muon data was larger than 5 standard deviations, and the corresponding 3-D density inversion compared well with drill assay data from the deposit.

1. Introduction

1.1. Muon Tomography

Muon radiography is a means of inferring density by measuring the attenuation of muon (a type of elementary particle) flux through matter. Muon tomography uses tomographic methods to derive three-dimensional (3-D) density maps from multiple muon flux measurements. This article reports on using muon radiographic and tomographic techniques to image density contrasts and reconstruct anomalous density distributions in searching for deep, compact ore bodies.

Measurements of the muon flux were first used by George (1955) to measure the overburden of a railway tunnel and by Alvarez et al. (1970) in searches for hidden chambers within pyramids. More recently, muon radiography has been used in volcanology (Ambrosi et al., 2011; Lesparre et al., 2012; Nagamine et al., 1995; Marteau et al., 2012; Tanaka et al., 2007). Muon tomography has been used in mineral exploration (Bryman et al., 2014; Bryman et al., 2015) and has also been considered for industrial and security applications (Cecchia, 2016).

Cosmic ray muons arise from high-energy interactions between cosmic rays (primarily protons, alpha particles) and atoms in the Earth's atmosphere. Due to their relatively long half-life and high mass, muons created in the upper atmosphere with energy larger than a few gigaelectron volts have a high probability of surviving as they travel through air and even deep underground at nearly the speed of light. The flux of muons incident from all angles on the surface of the Earth is about 1 cm⁻² · min⁻¹ (Beringer et al., 2012). One heuristic model of the muon intensity at sea level is due to Gaisser and Stanev (2000):

$$\frac{dN_{\mu}}{dE_{\mu} d\Omega} \approx \frac{0.14 E_{\mu}^{-2.7}}{\text{cm}^2 \cdot \text{s} \cdot \text{sr} \cdot \text{GeV}} \times \left(\frac{1}{1 + \frac{1.1 E_{\mu} \cos\theta}{115 \text{ GeV}}} + \frac{0.054}{1 + \frac{1.1 E_{\mu} \cos\theta}{850 \text{ GeV}}} \right), \tag{1}$$

where E_{μ} is the muon energy in gigaelectron volts and θ is the zenith angle of the muon trajectory with respect to vertical. This model has been modified more recently by Tang et al. (2006), and another model for the vertical muon flux has been proposed by Hebbeker and Timmermans (2002). CRM Geotomography Technologies, Inc. (CRM), has combined these parametrizations in a global fit that takes more recent experimental data into account (see Figures 1 and 2).

Muons lose energy as they pass through matter via ionization, bremsstrahlung, pair production, and other energy loss mechanisms at low energies (Beringer et al., 2012; Groom et al., 2001). Theoretical calculations for the various processes are well advanced (e.g., Beringer et al., 2012; Kelner et al., 1995; Kokoulin & Petruhin, 1997) and have been implemented in a number of muon transport codes (Agostinelli et al., 2003; Chirkin & Rhode, 2004; Kudryavtsev, 2009; Sokalski et al., 2001). Interfacing the sea level flux model with muon transport

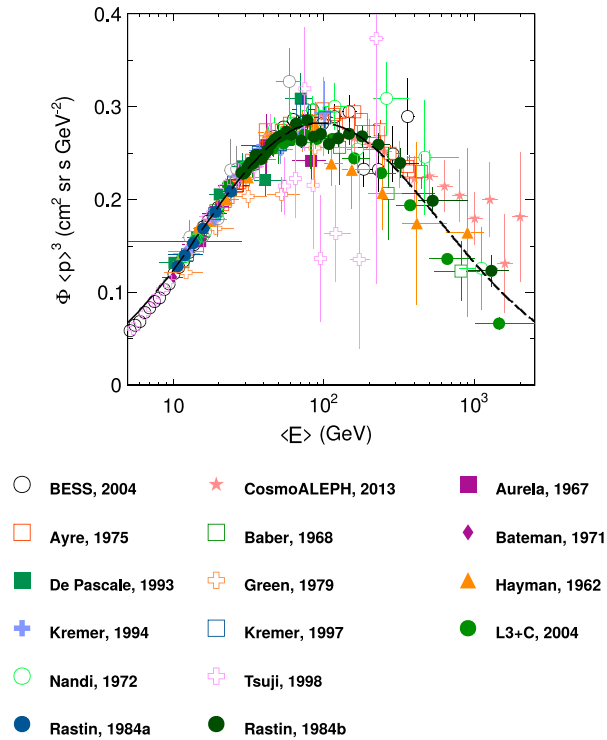


Figure 1. CRM's global fit (dashed curve) of the vertical muon intensity versus muon energy at sea level, compared to a variety of data sets published from the 1960s to 2010s (Aurela & Wolfendale, 1967; Ayre et al., 1975; Baber et al., 1968; Bateman et al., 1971; Haino et al., 2004; Muller & Schmelling, 2013; Grupen et al., 2007; De Pascale et al., 1993; Green et al., 1979; Hayman & Wolfendale, 1962; Kremer et al., 1999; Nandi & Sinha, 1972; Achard et al., 2004; Rastin, 1984; Tsuji et al., 1998). CRM = CRM Geotomography Technologies, Inc.

codes allows one to develop a model for making precise predictions for the muon intensity I underground as a function of the opacity \mathcal{O} between the sensor and the surface. Opacity is defined as the mass traversed along the muon path from the surface to the sensor:

$$\mathcal{O} = \int_{\text{path}} \rho(x, y, z) d\ell, \quad (2)$$

where $\rho(x, y, z)$ is the 3-D distribution of rock density, and \mathcal{O} is in units of grams per square centimeter, or meters of water equivalent (m w.e., hg/cm²). Using the inverse model I^{-1} , one is then able to infer an opacity \mathcal{O} from a measured I . The relationship between muon intensity I and the overburden opacity \mathcal{O} is shown in Figure 3.

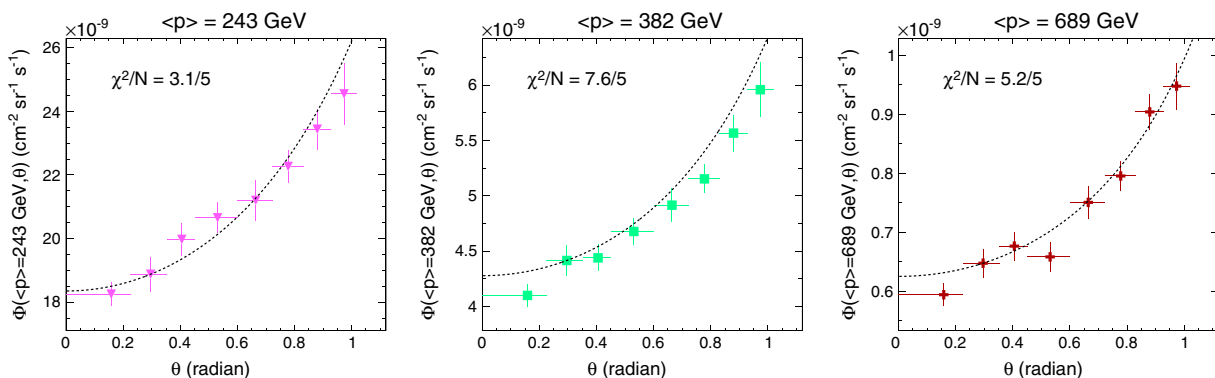


Figure 2. CRM's global fit as a function of the zenith angle of the muon trajectory, compared to L3+C data (Achard et al., 2004) in the momentum ranges most applicable to the McArthur River survey. Note that the CRM fit in these figures is scaled by a single factor, because there is an overall deficit in the L3+C measurements compared to the CRM fit (see Figure 1). The dependence on theta is unaffected by this flat scaling. CRM = CRM Geotomography Technologies, Inc.

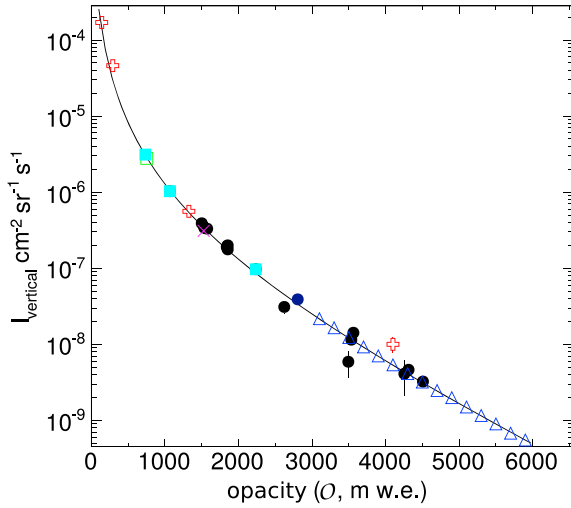


Figure 3. CRM's global fit of the vertical muon intensity versus opacity (which is approximately $2.7 \times$ depth underground, in units of meters of water equivalent, compared to a variety of data sets (Aglietta et al., 2005; Crouch, 1987). The theoretical model is for the standard rock formula defined in Groom et al. (2001) and uses the muon physics simulation in Geant4 (Agostinelli et al., 2003). Muons with total energy greater than 105 MeV (the muon rest mass) are included in the calculation of intensity at a given depth. CRM = CRM Geotomography Technologies, Inc.

Using the CRM muon tracking sensor (see section 1.2), trajectories for all muons passing through the sensor are measured and recorded. This allows one to generate maps of muon intensity, in which each pixel represents the measured intensity within a unit of solid angle. This intensity map can be compared to a reference map derived from an intensity model using a priori geological knowledge (e.g., a reference assuming a simple half-space density distribution). The number of muons passing through the detector within a given time period follows a Poisson distribution. A statistical interpretation of any deviation between the reference and measured intensity in each bin can therefore be determined by

$$p \equiv \begin{cases} \sum_{k=0}^N P(k; \lambda) & \text{if } N \geq \lambda \\ 1 - \sum_{k=0}^N P(k; \lambda) & \text{if } N < \lambda \end{cases}$$

$$\mathcal{Z} \equiv \sqrt{2} \operatorname{erf}^{-1}(2p - 1) \cdot \operatorname{sgn}(\lambda - N), \quad (3)$$

where $\lambda = I_{\text{reference}} \times \Delta t$ is the expected number of muons from the reference model, P is the Poisson distribution function, N is the observed number of muons, and \mathcal{Z} is the corresponding quantile of a standard normal distribution. Large positive values of \mathcal{Z} indicate a statistically significant higher opacity (lower intensity) unaccounted for in the reference geological model, whereas large negative values indicate a lower opacity (higher intensity). Images in which \mathcal{Z} is represented by a color (or $|\mathcal{Z}|$ in gray scale) in each pixel (region of solid angle) are useful 2-D visualizations

for identifying anomalous density within the muon sensor field of view. Examples of these images are shown in Figure 4.

By measuring the muon intensity at various angles and from various locations, one can infer a set of corresponding opacity measurements. The set of measurements $\{\mathcal{O}_i \pm \Delta\mathcal{O}_i\}$ can then be inverted to solve for the 3-D density distribution, $\rho(x, y, z)$ (see section 3.1). Anomalous regions in the spatial distribution of density can be used to target mineral exploration, among other applications. CRM has developed codes for inverting muon tomography data jointly with gravimetric data as well as incorporating a priori geological data, following work done by Oldenburg et al. (2010). This is described further in section 3.1.

1.2. Muon Sensors

The CRM muon sensor was developed for use in mines, so one of the key criteria is robustness to environmental variability and mechanical shock. The sensor is based on two *superplanes* of scintillator bars. Each

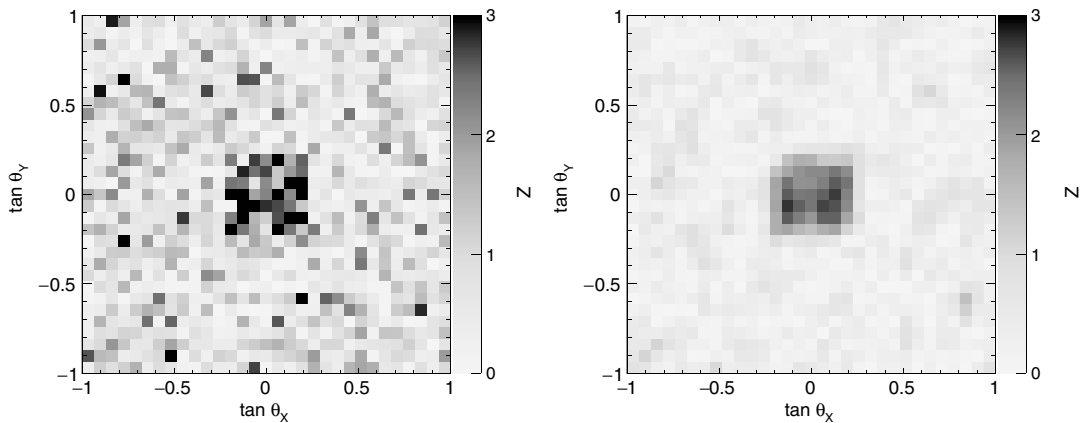


Figure 4. Example $|\mathcal{Z}|$ images for a simulated $50 \text{ m} \times 50 \text{ m} \times 20 \text{ m}$ cuboid (1 g/cm^3 contrast), 100 m above a muon sensor that is situated 400 m underground for 45 days. The images are shown with (left) and without (right) a sliding-window filtering algorithm applied. See section 2.2 for the definition of the image coordinates.

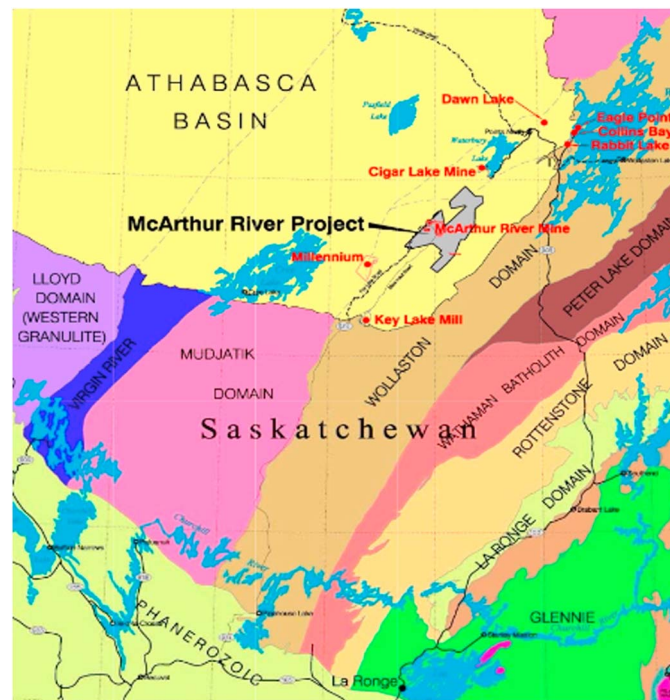


Figure 5. Geological domains of Northern Saskatchewan, Canada, from Bronkhurst et al. (2012).

superplane consists of two planes of bars oriented in orthogonal directions. The length and width of each plane are 2.1 and 1.1 m, respectively, and the thickness of each plane is about 6 cm. The scintillator bars are read out with wavelength-shifting optical fibers, which are connected to multichannel photomultiplier tubes, the signals of which are digitized by fast analog-to-digital converters. The data acquisition system is self-triggering. Any output from one of the analog-to-digital converters that is above a user-defined threshold is directed through a pipeline to a central collector, which applies a user-defined triggering logic to identify coincident pulses within a time window. The default triggering logic is to require an above-threshold pulse from each of the planes, and the time window for coincidence detection is 100 ns. By design, there is no triggering dead time in the sensor.

The sensor is enclosed in an aluminum shell, within which there are temperature and humidity controls and shock isolation mounts. Temperature, humidity, photomultiplier tube high voltage, trigger rates, and other monitors are read out and stored at intervals of a few seconds with the slow controls system. The only data used are those acquired when the slow control monitors indicate stable operation.

Once a candidate event is identified by the central collector, the digitized pulses are sent to a backend computer to be saved for offline processing. This computer is connected to the mine network, so the sensor can be queried remotely, and data can be offloaded and analyzed while the survey is being performed. The first stage of the processing is to apply quality criteria to the pulses to ensure stable pedestals and that each pulse shape is consistent with that produced by an ionizing particle. Pulses are grouped into hits, which form 3-D space points in the detector from which candidate tracks are then built. Quality criteria are also applied to the hits and to the tracks. These selection criteria are derived from simulations and open sky data testing. Each hit must contain a minimum charge (scintillation light yield), and at least one half of the hits in a track must contain a higher minimum charge. The sum of the hit charge in the track must be above another minimum threshold. Events containing multiple track candidates are vetoed (ambiguity from cross talk is taken into account in this veto). The track reconstruction algorithm is proprietary and achieves a spatial resolution about 10 times smaller than the pitch of the scintillator bars. The resolution and efficiency of each sensor is established using an auxiliary sensor. The detector performance was cross checked after transportation to and installation at the McArthur River mine to ensure that no misalignment or damage occurred. The angular resolution of the sensors used in this analysis is 10–13 mrad (depending on the muon angle), and the overall efficiency for identifying muons that pass through the detector, after applying all the data quality criteria, is > 90%. The live time of the sensors is > 99%.

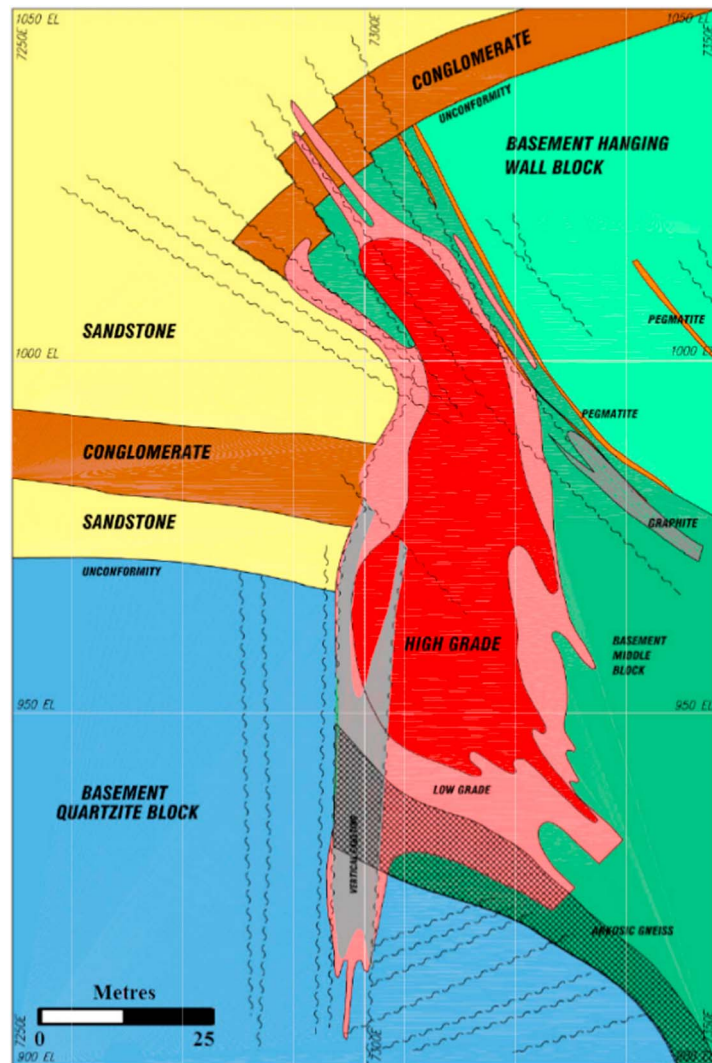


Figure 6. Typical geological section of the McArthur River uranium deposit, looking northeast. Taken from Bronkhurst et al. (2012).

1.3. Geological Setting

1.3.1. Regional Geology

The Athabasca region of northern Saskatchewan hosts the unconformity-related uranium deposits associated with the Athabasca Basin. The crystalline basement underlying the eastern part of the Athabasca Basin consists of complexly deformed and strongly metamorphosed igneous and supracrustal rocks of the Wollaston and Mudjatik Domains (see Figure 5). These crystalline basement rocks are unconformably overlain by the undeformed lower Paleoproterozoic to Mesoproterozoic Athabasca Group that consists mainly of sandstone with minor siltstone and conglomerate. The numerous Athabasca high-grade unconformity-type uranium deposits, including the McArthur River deposit, are hosted by the rocks at the vicinity of the sub-Athabasca unconformity, in both sandstone and basement. These deposits are related to sandstone-basement fluid interactions the locations of which were constrained broadly by basement structural corridors hosted by Wollaston Group graphitic pelitic gneiss and containing brittle faults (Jefferson et al., 2007a, 2007b; Hoeve & Sibbald, 1978; Hoeve & Quirt, 1984).

1.3.2. McArthur River Uranium Mine

The McArthur River uranium deposit, discovered by surface drilling of a geophysical electromagnetic target in 1988, is located approximately 500 m below the surface in the southeastern part of the Athabasca Basin. It has a proven and probable reserve of 1.053 million tonnes of ore at an average grade of about 15% uranium oxide (U_3O_8) for more than 150×10^6 kg pounds of U_3O_8 (Bronkhurst et al., 2014). It is the richest and

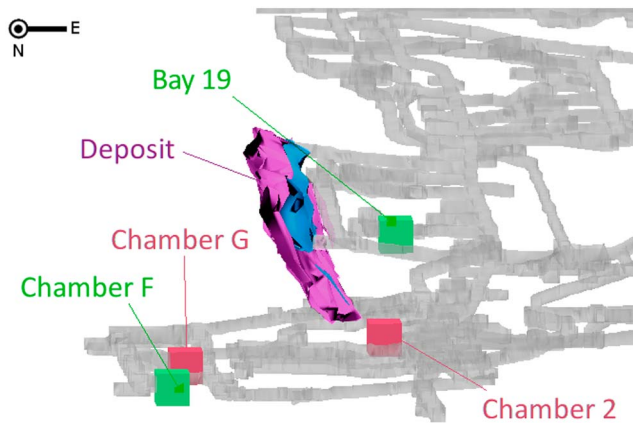


Figure 7. The McArthur River Zone IV North uranium deposit and the nearby mine workings. Also denoted are the locations of the muon tracking sensors used in the survey (described in section 2.1). Note that the muon sensors depicted are not to scale.

largest unconformity-related uranium deposit in the world, owned by Cameco Corporation (70%) and AREVA Resources Canada Inc. (30%), and operated by Cameco Corporation. The McArthur River uranium mineralization occurs at depths between 500 and 640 m around the unconformity between the host rocks of the Athabasca Group sandstone and basement metasedimentary gneisses. Commercial production at the mine was started on 1 November 2000. Since then, more than 100×10^6 kg of U_3O_8 have been produced (Bronkhorst et al., 2012).

The deposit is not surrounded by an extensive alteration halo common to other unconformity-associated uranium deposits (Jefferson et al., 2007a, 2007b), due to the presence of extensive premineralization silicification in the sandstone. However, lithological contrasts with associated different rock properties are present in the basement, with graphitic pelitic gneiss forming a strong electromagnetic conductor within a reverse fault system (the P2 fault) contrasting with nongraphitic lithologies. The P2 fault system offsets the unconformity by up to 80 m, with pelitic (with or without graphite) gneisses occurring in the hanging wall and garnet-cordierite pelitic gneisses in the footwall. Metaquartzite is present both above and below the pelitic gneisses. Similarly, the silicified zones in the Athabasca sandstone contrast with nonsilicified equivalents.

The uranium mineralization at McArthur River is hosted by Athabasca sandstones (Manitou Falls Formation) within the sandstone wedge footwall of the P2 fault, as well as in basement rocks also in the P2 footwall (Ng et al., 2013). Nine distinct mineralized zones have been identified at the McArthur River deposit, with most of the mineralization being located within the P2 graphitic fault system in the vicinity of the unconformity (see Figure 6; Bronkhorst et al., 2012). In this study, the Zone IV North region of the deposit was imaged using muon tomography. At the time the muon tomography survey was performed, extensive mining had not yet begun in this zone and the geometry of the deposit and accessible mine workings was also favorable. The Zone IV region had also been carefully studied from extensive drill core data, including detailed lithography, uranium concentration, density (measured and estimated), and water saturation were available. However, only sparse data were available for the dominant sandstone units located above the deposit. A view of the Zone IV North deposit and the nearby mine workings is shown in Figure 7.

2. Data Acquisition

Muon tomography data were acquired in three phases during the period from late September 2015 to December 2016. The CRM muon tracking sensors were installed in various positions with differing levels of ongoing mining activity and were connected to the mine network to facilitate remote data offloading and sensor configuration. Onboard environmental controls and shock absorbers ensured that nearby mining activity

Table 1

Locations of the detectors used in this survey, along with distance from the detector to the surface and the deposit, exposure time for the detector, detector active area, and orientation of the detector with respect to vertical

Phase	Location	ID	$d_{\text{surface}}, d_{\text{deposit}}$ (m)	Exposure (days)	Active area (m ²)	Muon flux (s ⁻¹)	Orientation
1	Chamber 2	1	599, 59	143	2.26	7.5×10^{-3}	0°
1	Chamber G	2	599, 85	83	—	7.6×10^{-3}	0°
2	Bay 19	1	542, —	66	—	1.1×10^{-2}	0°
2	Chamber G	1	599, 85	68	—	7.8×10^{-3}	0°
2	Chamber F	2	597, 86	65	—	7.6×10^{-3}	0°
3	Chamber 2	1	599, 59	70	—	7.7×10^{-3}	15°
3	Chamber 2	2	599, 61	54	—	7.5×10^{-3}	0°

Note. The orientation shown here is only approximate.

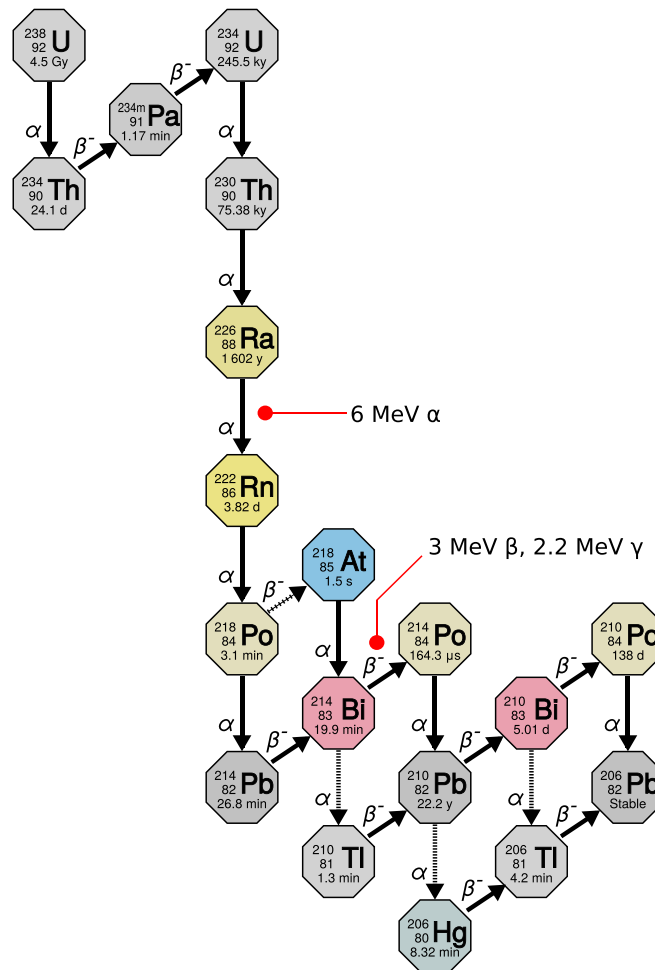


Figure 8. The decay chain for ^{238}U , including the decay mechanisms for each transition. The highest-energy α , β , and γ particle emitted throughout the decay chain is also indicated.

did not negatively impact sensor operation, but periodic power instabilities resulted in some unexpected interruptions that stretched out the data acquisition time.

2.1. Sensor Configuration

Two CRM muon tracking sensors were used in the survey, located at four distinct locations depicted as Chamber G, Chamber F, Chamber 2, and Bay 19 in Figure 7 and detailed in Table 1. In Phase I of the survey, the sensors were located at position Chamber G and Chamber 2, respectively, and the position and orientation of each sensor were recorded with mine surveying equipment. One of the sensors was positioned at Chamber F, and the other sensor at Bay 19 and then Chamber G in Phase II of the survey. In Phase III, the sensors were both positioned at Chamber 2 but with different orientations to the Zone IV deposit. The configuration of sensors was chosen to optimize sensitivity and imaging capability, by providing views of the deposit from multiple locations and orientations (i.e., Chambers 2, G, and F below the deposit), and to constrain the density of the sandstone (i.e., Bay 19 above the deposit) since the muon intensity depends on the cumulative opacity along the muon path to the surface. In this configuration, the muon sensors imaged about 1 km^3 of rock.

2.2. Data Processing and Quality

As described in section 1.2, the CRM muon sensors are spatially segmented into channels, each of which contributes to a global data stream that is processed in real time by a coincidence algorithm. The coincidence algorithm triggers a processing unit to record a time window of the data stream to disk if a configurable coincidence logic is satisfied. This data stream is processed offline to build candidate muon trajectories that must pass a set of quality selections. The set of selected muon trajectories are binned according to their respective directions in the mine coordinate system

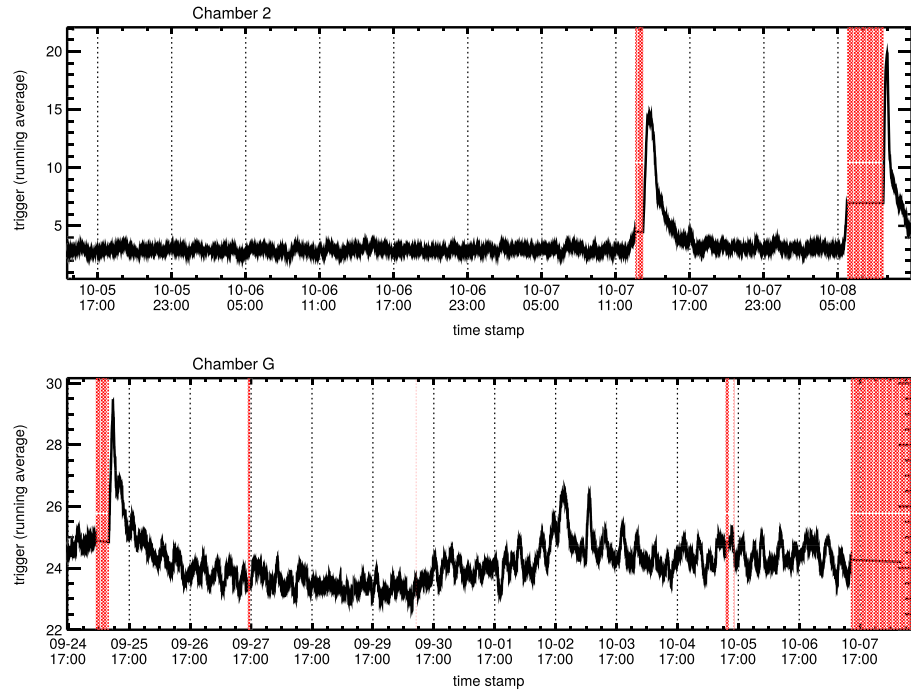


Figure 9. Sample raw data rate time series recorded by the sensors in Chamber 2 and Chamber G in Phase I of the survey. The red hatched blocks indicate periods in which the power was disabled in the mine. Immediately after prolonged outages there is a spike in the data rate because of radon pooling in the mine drifts as the ventilation system is shut down, followed by a roughly exponential decay as the radon dissipates. Note that the horizontal time axes are not the same. Periods with largest variability are shown as examples here. The marked difference in the baseline rate between the two sensors is due to a known large difference in the background radiation between the two sensor locations. The vertical axis is counts per second.

$$\begin{aligned} \tan \theta_x &= \frac{\Delta x}{\Delta z} \\ \tan \theta_y &= \frac{\Delta y}{\Delta z}, \end{aligned} \tag{4}$$

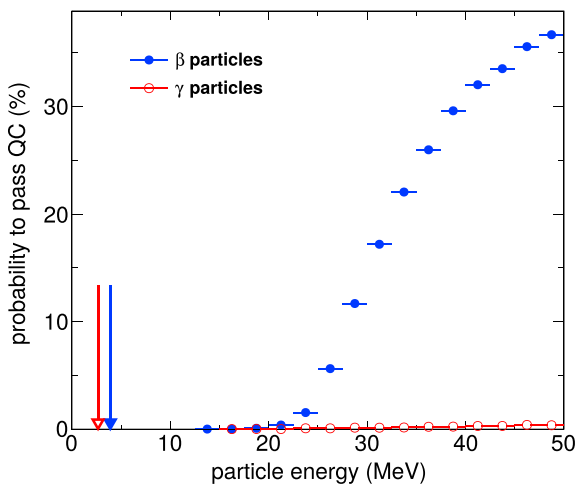


Figure 10. The probability for a β or γ particle to create a signature in the detector that passes the muon tracking quality criteria, as a function of the particle energy in the simulation. The highest energy β and γ particles expected from the ^{238}U decay chain is denoted by the arrows.

where x is the easting coordinate, y is the northing coordinate, and z is depth such that $\tan \theta_x = \tan \theta_y = 0$ is pointing straight up to the surface. Each data bin constitutes an inverted pyramidal cone extending from the sensor to the surface, within which solid angle the muon trajectories are collected. These binned data constitute a muon counts map, or *sensor image*, that can be compared to a map from synthetic data from a reference simulation (cf. section 1.1).

Given the unique radiation environment of a high-grade uranium mine, special care was taken to ensure that the muon sensor images were not contaminated by gamma, beta, and other particle backgrounds. There are a number of radioactive decay chains known to be relevant at McArthur River, primarily ^{238}U and to a lesser extent ^{235}U . The complex decay chain for ^{238}U is shown in Figure 8. The International Atomic Energy Agency database identifies the highest energy decay products from ^{238}U (as denoted in Figure 8), as a 6-MeV α particle, a 3-MeV β particle, and 2.2-MeV γ particle. No radioactive emission from ^{235}U has higher energy.

Basic calculations indicate that the β and γ particles both have a reasonable probability of penetrating the aluminum shell of the muon sensors and giving rise to a signal in the sensor components, whereas α particles

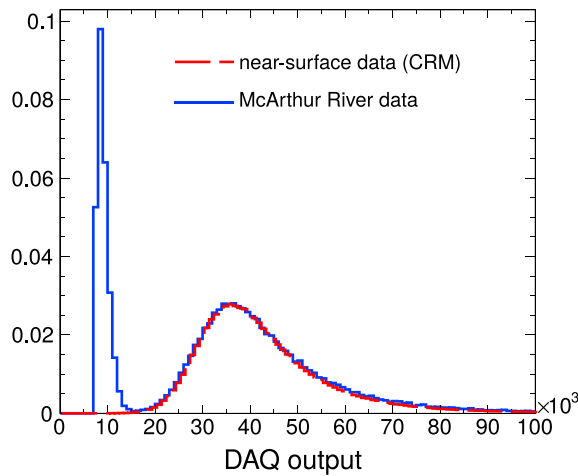


Figure 11. The distribution of a data acquisition (DAQ) system output for events with a high purity of muons collected at a CRM test facility (near-surface data) and collected at McArthur River. For reference, the nominal quality control selection requires this value to be greater than 17,000. Note that normalization in these distributions is arbitrary. CRM = CRM Geotomography Technologies, Inc.

number of data quality criteria are applied in order to identify the passage of high-energy muons through the detector and to reconstruct the muon trajectory. The criteria are designed to remove spurious signals from noise and other backgrounds, while maintaining a high efficiency for muons. The probability for a β or γ particle to be identified wrongly as a muon in the detector, as a function of the β or γ energy, is shown in Figure 10.

are stopped in a short distance of air and in only the few millimeters of the aluminum enclosure around the sensors. It is therefore an open question about whether the former will generate a signal sufficient to trigger an event recorded in the muon detector and fake a muon occurrence, thereby adding a background noise level to the measured muon flux. This question was investigated using the particle physics simulation engine Geant4 (Agostinelli et al., 2003). A diffuse cloud of background particle emissions was modeled around the detector. The simulation indicated that the β and γ backgrounds are sufficient to significantly increase the raw data rate of the detector. It is validated by a simple calculation using formulae from Beringer et al. (2012), for example. The effect of radiation on the raw data rate was also noticed in the recorded sensor data, as shown in Figure 9. It is important to note here that the raw data rate is expected to be dominated by nonmuon sources because the sensor trigger thresholds (the configuration for what sensor signals to record to disk for offline processing) are deliberately kept very low, to facilitate offline inspection of data quality and to maximize muon detection efficiency.

Further studies with Geant4 (Agostinelli et al., 2003) indicated that the nonmuon particle background was negligible when using the CRM muon sensor and data quality control algorithms. In the offline processing, a

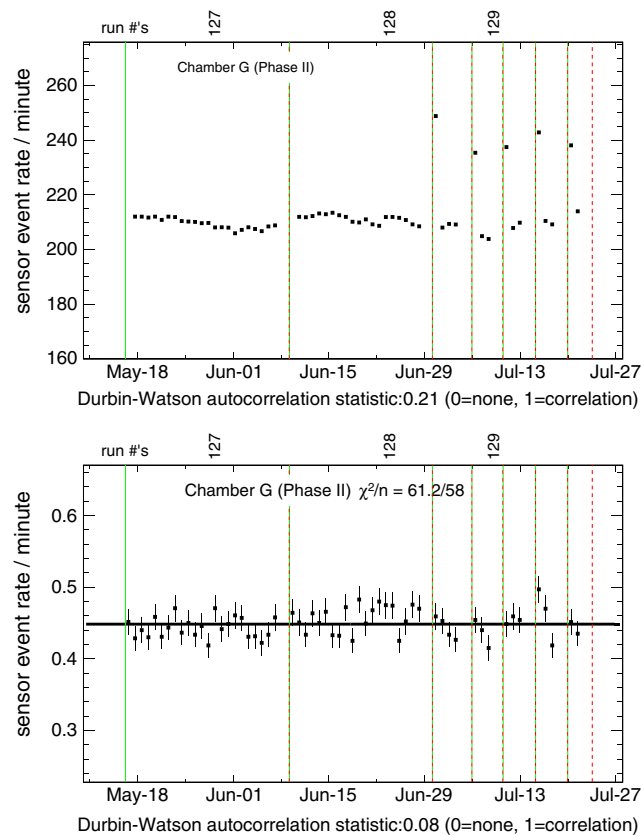


Figure 12. Raw trigger data rate for the sensor in Chamber G (top) for the duration of Phase I, and the event rate after applying data quality criteria (bottom). The Durbin-Watson statistic is denoted for each time series and is consistent with no temporal correlation after the data quality selections are applied.

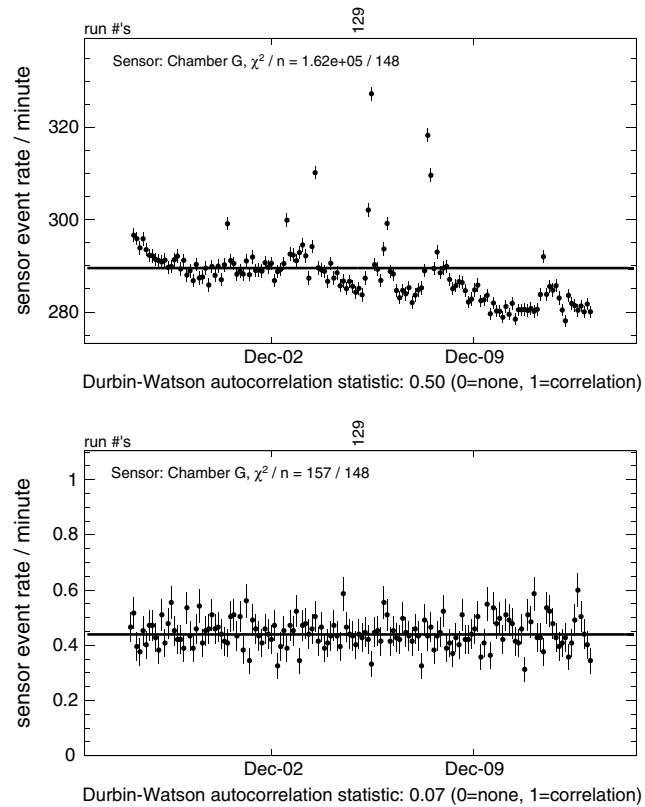


Figure 13. Raw trigger data rate for the sensor in Chamber G (top) for a data-taking period, and the event rate after applying data quality criteria (bottom). The Durbin-Watson statistic is denoted for each time series and is consistent with no temporal correlation after the data quality selections are applied. The χ^2/n for a fit to a constant is also shown for reference in both cases.

This indicates that after applying default data quality criteria, any contribution from α , β , and γ backgrounds at McArthur River is removed. This is also seen in the distribution of one of the data acquisition (DAQ) system outputs for triggered events without all of the data quality control criteria applied, shown in Figure 11. A sample of high purity cosmic ray muons is shown from data taken at a CRM test facility and compared to the distribution taken from sensors at McArthur River. There is a clear spike at low values in the McArthur River, consistent with low-energy background radiation.

This was confirmed by cross checks performed with the data, by comparing data from sensors in different locations with known differences in background radiation, and also by looking at temporal correlations to the changing radiation background (measured independently). The data rate recorded by the detectors is

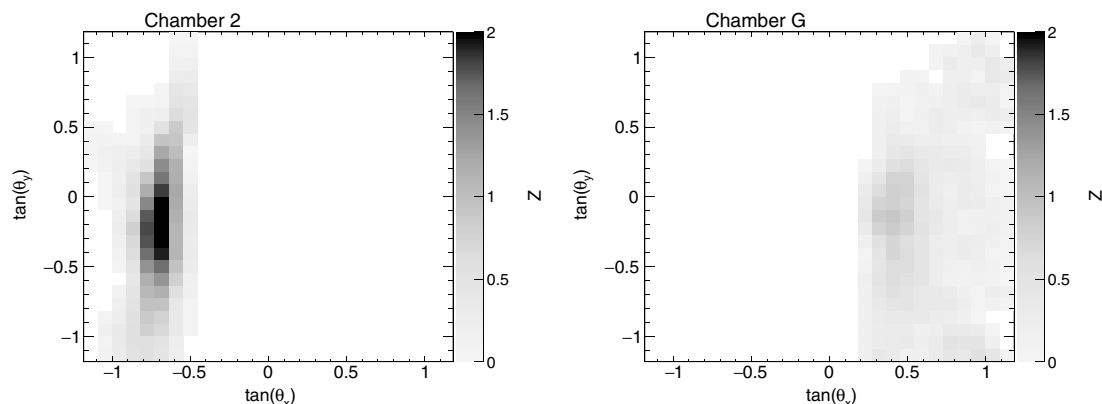


Figure 14. Expected anomalous Z in the muon counts maps from synthetic data for sensors in Chamber 2 (left) and Chamber G (right).

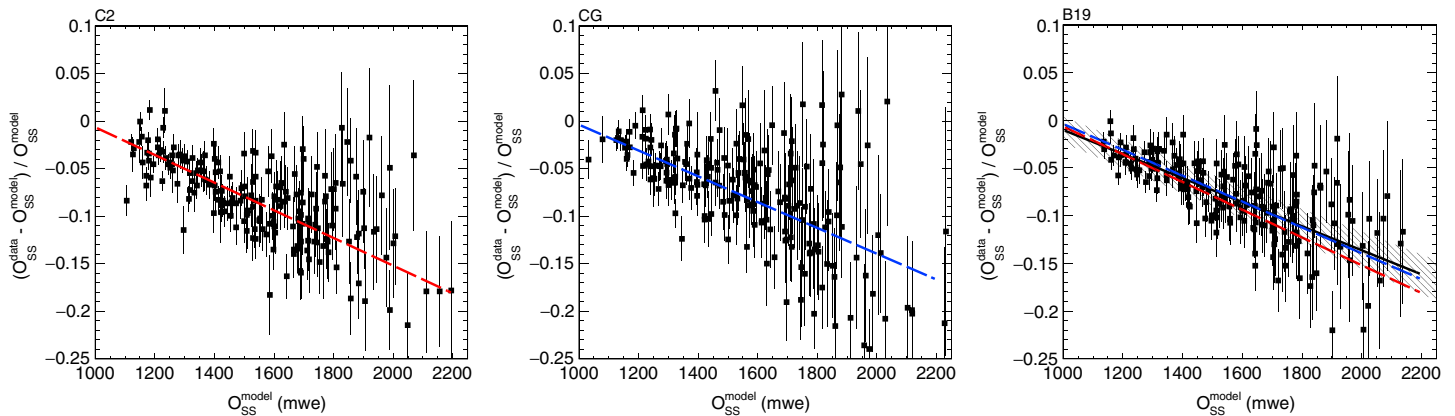


Figure 15. Relative difference between measured and modeled (expected) opacity versus the modeled opacity from the sandstone only for (left) Chamber 2, (middle) Chamber G, and (right) Bay 19 data. The same trend is observed in all the data sets, but only the Bay 19 data are used to derive the correction. Comparison between the three trends is shown in the Bay 19 subfigure, along with the hatched area indicating the 68% uncertainty band around the fitted trend.

shown in Figure 12 before and after applying the standard data quality criteria. Since the β and γ background contamination fluctuates significantly over time (as shown in the raw data rate time series in Figure 9), then if there was any residual contamination after the data quality selections, there would be a time series correlation in the final muon event rates. This is quantified with the Durbin-Watson test, as indicated in Figure 12, which shows that no evidence for such correlation is present after the quality criteria are applied. This is also shown on a much finer timescale for a sample data collection period from Chamber G in Figure 13.

The seasonal variations of the muon flux described in Adamson et al. (2010) were not observed in these data, but the statistical uncertainties on the flux within seasonal time windows were larger than the expected seasonal variations. The effect of different sea level intensity models, different muon physics codes for modeling the muon interactions with matter, and detector-related systematic uncertainties such as the sensor performance model or environmental dependencies have also been investigated. Although each of these systematic uncertainties give rise to global changes in the inferred underground density, none of them were found to be able to produce localized anomalies in the radiographic images such as would be expected from the presence of a dense ore body within the fields of view of the detectors. Finally, calculations for multiple scattering showed that $> 99\%$ of the scattering angle distribution for muons at 600 m underground is less than the width of a single pixel in the muon counts maps used in this analysis. Therefore, scattered muons could also be excluded as a relevant systematic uncertainty source for this study.

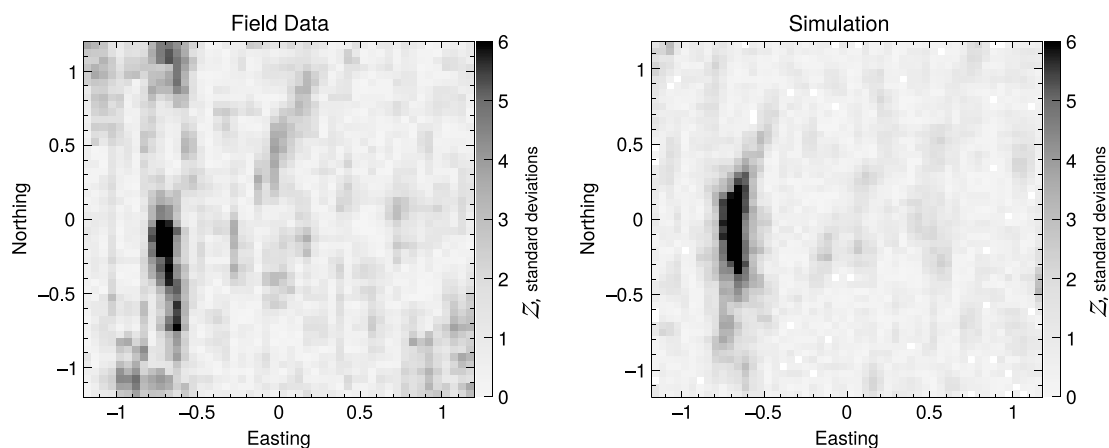


Figure 16. The anomalous $|Z|$ for the field data (left) compared to the ideal geological reference for Chamber 2 data. Also shown for comparison is the same calculation for synthetic data (simulation, right). In both images, the same sliding-window filtering algorithm is applied.

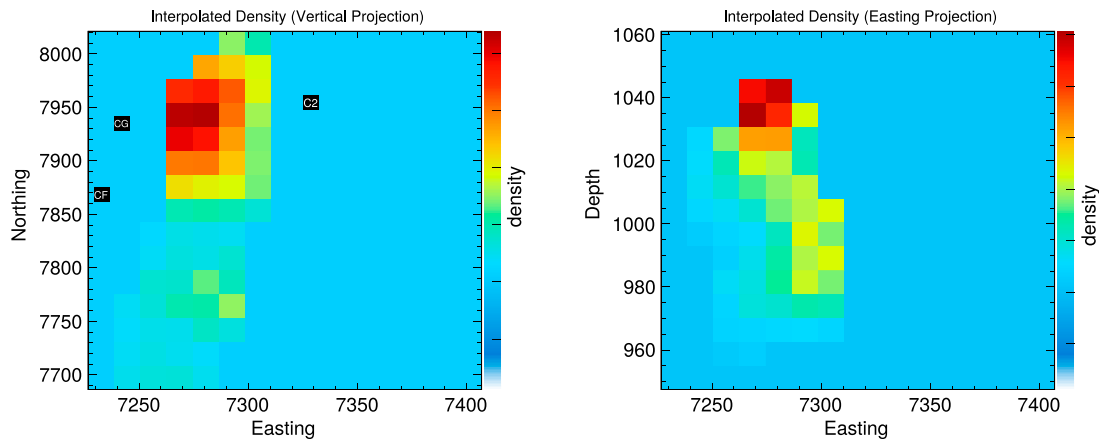


Figure 17. The density profile of the deposit, projected in the northing–easting (left) and depth–easting (right) planes. The variation in the density distribution is more than 0.5 g/cm^3 . The locations of the sensors are indicated in the northing–easting projection (left).

3. Data Interpretation and Results

In the interpretation of the muon tomography data, two reference geological models are employed. In both models, lidar topography and mine workings are incorporated, and the deposit is assumed to have the same properties as the surrounding host rock. The *simplified* model assumes a uniform host rock throughout the imaging volume, with density 2.55 g/cm^3 . The *ideal* model incorporates geological units with corresponding densities as defined from drill data near the P2 fault. The range in density among these geological units is 2.5 to 2.65 g/cm^3 .

In order to estimate the sensitivity of the survey to the deposit, synthetic muon sensor data were produced from a simulation in which the deposit model density was uniformly set corresponding to high-grade uranium ore. These synthetic data were compared to the ideal model prediction. The resultant synthetic images in Figure 14 indicate the expected Z in the muon counts maps arising from the presence of high-grade ore. It is clear that data acquired in Chamber 2 are expected to be most sensitive. This is due to the orientation of the ore body: muons traverse a longer path length through the deposit to the sensor in Chamber 2 than for sensors in Chambers G and F.

An unexpected global trend in the observed muon intensity versus depth underground was noticed early in data acquisition. In order to isolate the analysis of the local geology around the deposit from the dominant sandstone units above the fault, the data from the sensor in Bay 19 are used to correct the opacity model for the sandstone in situ. This correction is illustrated in Figure 15. Due to a paucity of drill data, the sandstone is treated uniformly as *standard* rock (Groom et al., 2001) in both the ideal and simplified models, whereas density and chemical composition deviates throughout the sandstone overburden. Differences between the

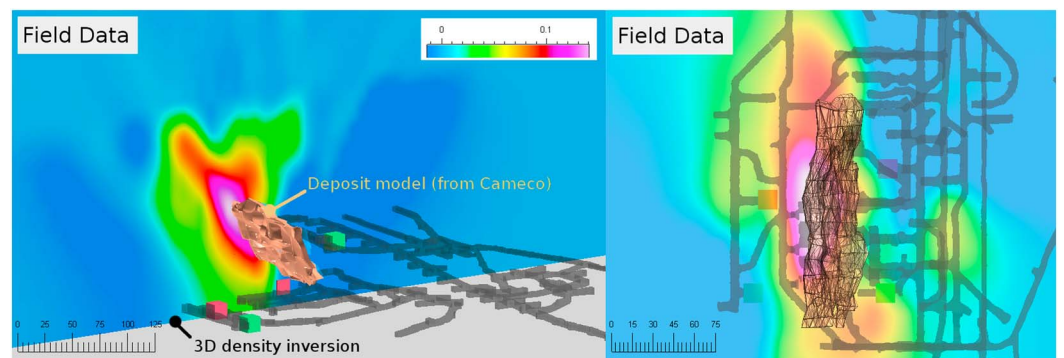


Figure 18. Slices through the density distribution derived by inverting muon tomography data acquired from the CRM sensors in Chambers 2, G, and F and Bay 19. The view on the left is in the northing direction, whereas the semitransparent view on the right is looking downward. The color scale indicates the variation in anomalous density (g/cm^3) with respect to the reference uniform density. CRM = CRM Geotomography Technologies, Inc.

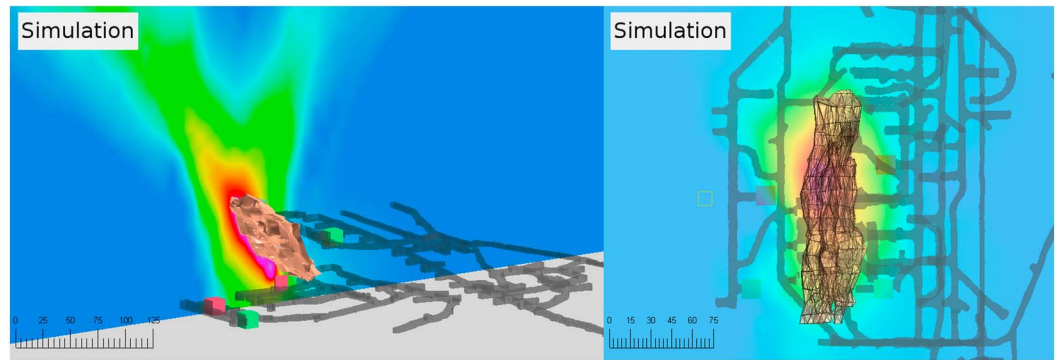


Figure 19. Slices through the density distribution derived by inverting synthetic muon tomography data. The view on the left is in the northing direction, whereas the semitransparent view on the right is looking downward. Note that the color map for the density distribution is the same as in Figure 18.

idealized rock and the actual sandstone give rise to an observed global trend. Note that > 80% of the opacity is composed of the sandstone, so mismodeling of the sandstone will dominate the subtler local variations around the deposit. Since the Bay 19 data are only sensitive to the sandstone above the deposit, it can be used to remove the global trend from the other data sets in Chambers 2, G, and F. It is important to note that the same global trend is observed in all the data, justifying the use of a correction derived from Bay 19 data. This analysis illustrates the importance of judicious placement of muon sensors in areas where the local geology is unknown. By doing measurements at multiple depths, a data-driven interpretation of the region of interest can be attained.

After applying the global correction, the anomalous $|\mathcal{Z}|$ is calculated from the data based on the ideal geological reference as shown in Figure 16. The same calculation is performed for the synthetic data set described above. Good correspondence between the field data and the synthetic data (simulation) is apparent. It is important to note that the synthetic data assume a uniform density distribution throughout the deposit, whereas in fact the grade and corresponding density is highly variable, as shown in Figure 17.

3.1. Three-Dimensional Density Inversion

In order to construct a 3-D density distribution from the muon tomography data, an inversion algorithm is used that minimizes a global function ϕ :

$$\min_{\rho(x,y,z)} \phi = \min_{\rho(x,y,z)} (\phi_D + \beta \cdot \phi_M), \quad (5)$$

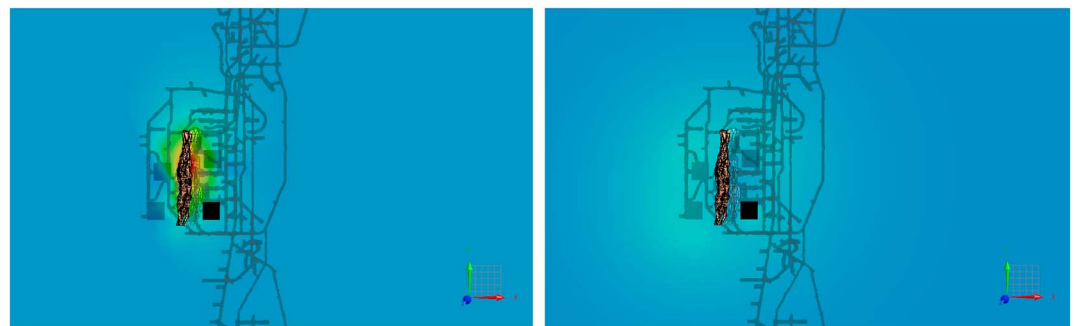


Figure 20. Three-dimensional distribution of anomalous density arising from assumed mismodeling of the effective sandstone density, derived by shifting the global trend correction parameter by 1σ (left), and the 3-D distribution from inverting synthetic data from the deposit model (right). The color scale in both images is the same.

where ϕ_D is a data misfit for the muon tomography data compared to the ideal reference model, and ϕ_M is a model objective function that ensures smoothness. These terms are defined as

$$\phi_D = \sum_{i \in \text{pixels}} \frac{\left(d_i - \sum_j G_{ij} \rho_j \right)^2}{\sigma_i^2} \quad (6)$$

$$\phi_M = \sum_{w=x,y,z} \alpha_w \int_V \left(\frac{\partial \rho}{\partial w} \right)^{q_w} dV + \alpha_r \int_V (\rho_0 - \rho)^p dV, \quad (7)$$

where G_{ij} is a very sparse matrix for the sensitivity of each i th pixel to the j th voxel in the image volume, σ_i is the uncertainty of data measurement d_i , α_w is a constant that penalizes roughness in each of the $w = x, y, z$ coordinates, and α_r is a constant that penalizes deviations from a reference model $\bar{\rho}_0$. Setting $\alpha_{r,x,y,z} = 0$ disables the respective parts of the model objective function. This method follows the work of Oldenburg et al. (2010), Davis and Oldenburg (2012), and Bryman et al. (2014). The exponents q_w and p are in the range (1, 2], with smaller values allowing for more complex (less smooth) models. The minimum of the global function ϕ is determined using the conjugate gradient minimization algorithm (Straeter, 1971).

Except for smoothness and a weak constraint on the absolute sandstone density > 100 m above Bay 19, no constraints are imposed on the density values determined in the inversion. The inversion algorithm is applied identically to both the synthetic data and the field data. Data from sensors in Chambers 2, G, and F as well as Bay 19 are used in the inversion. Slices through the resultant 3-D density distributions are shown in Figures 18 (field data) and 19 (synthetic data), along with the deposit model derived from drill core data. The compatibility of the density distributions for synthetic and field data is very good. With reference to the depth-easting projection in Figure 17, it is noteworthy that the high-density core is shifted upward in the field data with respect to the synthetic data (which assume a uniform density distribution in the simulation).

Sensitivity to the global trend correction described in section 3 is investigated as a source of systematic error on the 3-D density inversion. Synthetic data are produced with varied parameters in the global trend correction, and the same 3-D inversion as used on the field data is applied. The resultant apparent anomaly arising from uncertainty on the global correction is shown in Figure 20, and is compared to the 3-D density distribution from inversion of synthetic data from the deposit model. This demonstrates that systematic uncertainty in the global trend correction does not mimic the deposit signature, either in magnitude or location.

Acknowledgments

We acknowledge the Cameco Corporation for providing logistical and operational support throughout the data acquisition period, as well as detailed geological information. We are indebted to Mufaro Chivasa, Remi Labelle, Chunyong Pang, Andrew Laarz, Tara Maccan, and Garnet Wood from Cameco. We extend our sincere thanks to Robert Hearst, David Quirt, and Trevor Allen from Areva for their input and assistance in the McArthur River muon tomography project, and we acknowledge the financial support of the Areva Corporation. We also thank TRIUMF Innovations (formerly Advanced Applied Physics Solutions) and the National Research Council of Canada (NRC) Industrial Research Assistance Program (IRAP) for their support of CRM Geotomography Technologies. Finally, we give credit to Brian Powell, the geophysicist from Cameco who suggested applying muon tomography to uranium exploration more than 10 years ago. Due to the commercial sensitivity of measurements made in this active uranium mine, the data used and produced in this analysis may not be released. For specific inquiries regarding the data, please contact the authors.

4. Discussion and Conclusions

Tomographic imaging with muons has been used to image the high-grade McArthur River uranium deposit in the Athabasca Basin. This work represents the first such survey ever performed. The resultant muon tomography data exhibit very good correspondence to the drill data and geological models, and the corresponding 3-D density inversion of the muon tomography data maps well to the deposit profile. Analysis of the muon data has provided two key lessons:

1. Data-driven interpretation of the geology within a region of interest can be achieved from cross comparisons of sensor data at multiple depths.
2. Detector design and muon track discrimination algorithms are important where background radiation can be significant.

Finally, regardless of the efficacy of muon tomography demonstrated in this survey, the future of this technology in mineral exploration and other underground applications lies in the development of a robust borehole muon sensor, because the sensor used in this survey can only be used where existing mine infrastructure is in place. This will be the subject of future work.

References

- Achard, P., Adriani, O., Aguilar-Benitez, M., van den Akker, M., Alcaraz, J., Alemanni, G., et al. (2004). Measurement of the atmospheric muon spectrum from 20 to 3000 GeV. *Physics Letters B*, 598, 15–32. <https://doi.org/10.1016/j.physletb.2004.08.003>
- Adamson, P., Andreopoulos, C., Arms, K. E., Armstrong, R., Auty, D. J., Ayres, D. S., et al. (2010). Observation of muon intensity variations by season with the MINOS Far Detector. *Physical Review D*, 81(1), 12001. <https://doi.org/10.1103/PhysRevD.81.012001>
- Aglietta, M., Alpat, B., Alyea, E. D., Antonioli, P., Badino, G., Bari, G., et al. (2005). Muon 'depth-intensity' relation measured by the LVD underground experiment and cosmic-ray muon spectrum at sea level. *Physical Review D*, 58(9), 092005. <https://doi.org/10.1103/PhysRevD.58.092005>

- Agostinelli, S., Allison, J., Amako, K., Apostolakis, J., Araujo, H., Arce, P., et al. (2003). Geant4—A simulation toolkit. *Nuclear Instruments and Methods in Physics Research Section A*, 506, 250–303. [https://doi.org/10.1016/S0168-9002\(03\)01368-8](https://doi.org/10.1016/S0168-9002(03)01368-8)
- Alvarez, L., Alvarez, J. A., Anderson, F., El, B., James, B., Ahmed, F., et al. (1970). Search for hidden chambers in the pyramids using cosmic rays. *Science*, 167, 832–839.
- Ambrosi, G., Ambrosino, F., Battiston, R., Bross, A., Callier, S., Cassese, F., et al. (2011). The MU-RAY project: Volcano radiography with cosmic-ray muons. *Nuclear Instruments and Methods in Physics Research Section A*, 628, 120–123. <https://doi.org/10.1016/j.nima.2010.06.299>
- Aurela, A., & Wolfendale, A. (1967). The energy spectrum of cosmic-ray muons in the vertical direction. *Annales Academiæ Scientiarum Fennicæ, VI, no.*, 227.
- Ayre, C., Baxendale, J., Hume, C., Nandi, B., Thompson, M., & Whalley, M. (1975). Precise measurement of the vertical muon spectrum in the range 20–500 GeV/c. *Journal of Physics G: Nuclear Physics*, 1(5), 584–600.
- Baber, S., Nash, W., & Rastin, B. (1968). The momentum spectrum of muons at sea-level in the range 3–1000 GeV/c. *Nuclear Physics B*, 4, 539–48.
- Bateman, B., Cantrell, W., Durda, D., Duller, N., Green, P., Jelinek, A., et al. (1971). Absolute measurement of the vertical cosmic ray muon intensity at 3–50 GeV/c near sea level. *Physics Letters B*, 36, 144–148.
- Beringer, J., Arguin, J.-F., Barnett, R. M., Copic, K., Dahl, O., Groom, D. E., et al. (2012). Review of particle physics. *Physical Review D*, 86(1), 10001. <https://doi.org/10.1103/PhysRevD.86.010001>
- Bronkhorst, D., Mainville, A., Murdock, G., & Yesnik, L. (2012). (Cameco Corporation), McArthur river operation, Northern Saskatchewan, Canada National Instrument 43-101 Technical Report.
- Bronkhorst, D., Mainville, A., Yesnik, L., & Tang, B. (2014). (Cameco Corporation), Mineral reserves and resources—Cameco 2014 online annual report. Retrieved from https://www.cameco.com/annual_report/2014/mda/mineral-reserves-and-resources/
- Bryman, D., Bueno, J., & Jansen, J. (2015). Blind test of muon geotomography for mineral exploration. *ASEG Extended Abstracts*, 164, 1–3.
- Bryman, D., Bueno, J., Oldenburg, D., & Liu, Z. (2014). Bringing new physics to orebody imaging. *Society of Economic Geologists Special Publication*, 18, 235–241.
- Cecchia, P. (2016). Review of possible applications of cosmic muon tomography. *Journal of Instrumentation*, 11(12), C12072. <https://doi.org/10.1088/1748-0221/11/12/C12072>
- Chirkin, D., & Rhode, W. (2004). Propagating leptons through matter with muon Monte Carlo (MMC). arXiv:hep-ph/0407075.
- Crouch, M. (1987). An improved world survey expression for cosmic ray vertical intensity vs. depth in standard rock. In *Proceedings of International Cosmic Ray Conference* (pp. 165).
- Davis, K., & Oldenburg, D. (2012). Joint 3D of muon tomography and gravity data to recover density. In *ASEG Extended Abstracts 2012: 22nd Geophysical Conference* (pp. 1–4). <https://doi.org/10.1071/ASEG2012ab172>
- De Pascale, M., Morselli, A., Picozza, P., Golden, R. L., Grimani, C., Kimbell, B. L., et al. (1993). Absolute spectrum and charge ratio of cosmic ray muons in the energy region from 0.2 GeV to 100 GeV at 600 m above sea level. *Journal of Geophysical Research*, 98, A3.
- Gaisser, T., & Stanev, T. (2000). Cosmic rays. *The European Physical Journal C - Particles and Fields*, 15, 150–156. <https://doi.org/10.1007/BF02683416>
- George, E. (1955). Cosmic rays measure overburden of tunnel Commonwealth Engineer 455–457.
- Green, P., Duller, N., Magnuson, C., Choate, L., Sheldon, W., Osborne, A., et al. (1979). Absolute intensities of medium-energy muons in the vertical and at zenith angles 55°–85°. *Physical Review D*, 20, 1598–1607.
- Groom, D., Mokhov, N., & Striganov, S. (2001). Muon stopping-power and range tables, 10 MeV–100 TeV. *Atomic Data and Nuclear Data Tables*, 78, 183–356.
- Grupe, C., Hashim, N.-O., Jost, B., Maciuc, F., Luitz, S., Mailov, A., et al. (2007). Cosmic ray results from the CosmoALEPH experiment. *Nuclear Physics B - Proceedings Supplements*. In *Proceedings of the XIV International Symposium on Very High Energy Cosmic Ray Interactions* (pp. 175–176). <https://doi.org/10.1016/j.nuclphysbps.2007.11.014>
- Haino, S., Sanuki, T., Abe, K., Anraku, K., Asaoka, Y., Fuke, H., et al. (2004). Measurements of primary and atmospheric cosmic-ray spectra with the BESS-TeV spectrometer. *Physics Letters B*, 594, 35–46. <https://doi.org/10.1016/j.physletb.2004.05.019>
- Hayman, P., & Wolfendale, A. (1962). The momentum spectrum of cosmic ray muons near sea level in the momentum range 5–1000 GeV/c. *Proceedings of the Physical Society*, 80, 710.
- Hebbeker, T., & Timmermans, C. (2002). A compilation of high energy atmospheric muon data at sea level. *Astroparticle Physics*, 18, 107–27. [https://doi.org/10.1016/S0927-6505\(01\)00180-3](https://doi.org/10.1016/S0927-6505(01)00180-3)
- Hoeve, J., & Quirt, D. (1984). Mineralization and host rock alteration in relation to clay mineral diagenesis and evolution of the Middle-Proterozoic, Athabasca Basin, northern Saskatchewan, Canada. Saskatchewan Research Council. *SRC Technical Report*, 187, 187.
- Hoeve, J., & Sibbald, T. (1978). On the genesis of Rabbit Lake and other unconformity-type uranium deposits in northern Saskatchewan. *Canada: Economic Geology*, 73, 1450–1473.
- Jefferson, C., Thomas, D., Gandhi, S., Ramaekers, P., Delaney, G., Brisbin, D., et al. (2007a). Unconformity associated uranium deposits of the Athabasca basin, Saskatchewan and Alberta. *Geological Survey of Canada Bulletin*, 588, 23–67.
- Jefferson, C., Thomas, D., Gandhi, S., Ramaekers, P., Delaney, G., Brisbin, D., et al. (2007b). Unconformity-associated uranium deposits of the Athabasca Basin, Saskatchewan and Alberta. In W. Goodfellow (Ed.), *Mineral deposits of Canada: A synthesis of major deposit-types, district metallogeny, the evolution of geological provinces, and exploration methods* (Vol. 5, pp. 273–305). Canada: Geological Association of Canada Mineral Deposits Division Special Publication.
- Kelner, S., Kokoulin, R., & Petrukhin, A. (1995). About cross section for high-energy muon bremsstrahlung. Moscow Inst. of Technology.
- Kokoulin, R., & Petrukhin, A. (1997). Muon interactions and consequences in underground physics frontier objects in astrophysics and particle physics. *Proceedings of the Vulcano Workshop*, 57, 379.
- Kremer, J., Boezio, M., Ambriola, M. L., Barbiellini, G., Bartalucci, S., Bellotti, R., et al. (1999). Measurements of ground-level muons at two geomagnetic locations. *Physical Review Letters*, 83, 4241–4244. <https://doi.org/10.1103/PhysRevLett.83.4241>
- Kudryatsev, V. (2009). Muon simulation codes MUSIC and MUSUN for underground physics. *Computer Physics Communications*, 180, 339–46. <https://doi.org/10.1016/j.cpc.2008.10.013>
- Lesparre, N., Gibert, D., Marteau, J., Komorowski, J.-C., Nicollin, F., & Coutant, O. (2012). Density muon radiography of La Soufriere of Guadeloupe volcano: Comparison with geological, electrical resistivity and gravity data muons tomography applied to geosciences and volcanology. *Geophysical Journal International*, 190, 1008–1019. <https://doi.org/10.1111/j.1365-246X.2012.05546.x>
- Marteau, J., Gibert, D., Lesparre, N., Nicollin, F., Noli, P., & Giacoppo, F. (2012). Muons tomography applied to geosciences and volcanology. *Nuclear Instruments and Methods in Physics Research Section A*, 695, 23–28. <https://doi.org/10.1016/j.nima.2011.11.061>
- Muller, A.-S., & Schmelling, M. (2013). Final analysis of muon spectrum and charge ratio (CosmoALEPH). Private Communication.

- Nagamine, K., Iwasaki, M., Shimomura, K., & Ishida, K. (1995). Method of probing inner-structure of geophysical substance with the horizontal cosmic-ray muons and possible application to volcanic eruption prediction. *Nuclear Instruments and Methods in Physics Research Section A*, 356, 585–595. [https://doi.org/10.1016/0168-9002\(94\)01169-9](https://doi.org/10.1016/0168-9002(94)01169-9)
- Nandi, B., & Sinha, M. (1972). The momentum spectrum of muons at sea level in the range 5–1200 GeV/c. *Journal of Physics A: General Physics*, 5, 1384.
- Ng, R., Alexandre, P., & Kyser, T. (2013). Mineralogical and geochemical evolution of the unconformity-related McArthur River Zone 4 orebody in the Athabasca Basin, Canada: Implications of a silicified zone. *Economic Geology*, 108, 1657–1689.
- Oldenburg, D., Davis, K., & Kaminski, V. (2010). *Inversion for muon tomography*. Vancouver, BC, Canada: Unpublished Communication.
- Rastin, B. (1984). An accurate measurement of the sea-level muon spectrum within the range 4 to 3000 GeV/c. *Journal of Physics G: Nuclear Physics*, 10, 1609.
- Sokalski, I., Bugaev, E., & Klimushin, S. (2001). MUM: Flexible precise Monte Carlo algorithm for muon propagation through thick layers of matter. *Physical Review D*, 64(7). <https://doi.org/10.1103/PhysRevD.64.074015>
- Straeter, T. A. (1971). On the extension of the Davidon-Broyden class of rank one, quasi-Newton minimization methods to an infinite dimensional Hilbert space with applications to optimal control problems (PhD thesis), North Carolina State University. NASA-CR-111975.
- Tanaka, H., Nakano, T., Takahashi, S., Yoshida, J., Takeo, M., Oikawa, J., et al. (2007). High resolution imaging in the inhomogeneous crust with cosmic-ray muon radiography: The density structure below the volcanic crater floor of Mt. Asama, Japan. *Earth and Planetary Science Letters*, 263, 104–113. <https://doi.org/10.1016/j.epsl.2007.09.001>
- Tang, A., Horton-Smith, G., Kudryavtsev, V., & Tonazzo, A. (2006). Muon simulations for Super-Kamiokande, KamLAND, and CHOOZ. *Physical Review D*, 74(5).
- Tsuji, S., Katayama, T., Okei, K., Wada, T., Yamamoto, I., & Yamashita, Y. (1998). Measurements of muons at sea level. *Journal of Physics G: Nuclear and Particle Physics*, 24, 1805. <https://doi.org/10.1088/0954-3899/24/9/013>